Sensors & Actuators: B. Chemical 445 (2025) 138577

Contents lists available at ScienceDirect

Sensors and Actuators: B. Chemical

journal homepage: www.elsevier.com/locate/snb

Imidazole-amino modified organic-metal chalcogenide for enhanced recyclability and recovery rate in gas sensing

Wei Gong [a,b], Yu Pan [a,b], Yusheng Shi [a,*], Guane Wang [a,*], Gang Xu [a]

[a] State Key Laboratory of Structural Chemistry, Fujian Provincial Key Laboratory of Materials and Techniques toward Hydrogen Energy, Fujian Institute of Research on the Structure of Matter, Chinese Academy of Sciences, Fuzhou, Fujian 350108, P R China
[b] University of Chinese Academy of Sciences (UCAS), No. 19A Yuquan Road, Beijing 10049, P R China

ARTICLE INFO

Keywords:
Functional group
Structure-property relationship
Organic-metal chalcogenide
Gas sensing

ABSTRACT

Two-dimensional (2D) organic metal chalcogenides (OMCs) show promise for gas sensing due to their programmable active sites, but often suffer from slow recovery and poor cycling stability due to strong interactions between analyte and active site on OMCs. To optimize this issue, we rationally screened and identified the optimal active sites with tailored analyte interaction strengths. Theoretical screening identifies benzimidazole shows the lowest binding energy (-2.93 kcal/mol) with NO_2, enabling faster desorption. A new 2D OMC, AgBMT (BMT = 2-mercaptobenzimidazole), with long-range ordered benzimidazole covered on its surfaces was successfully synthesized. AgBMT exhibits exceptionally fast response (14 s) and recovery times (46 s) to NO_2. The recovery time is among the fastest levels reported for NO_2 sensors. The coefficient of variation (CV) value of AgBMT is 2.19 %, which is the lowest among reported NO_2 sensors with recovery times of less than 1 min. Moreover, AgBMT exhibits negligible response to humidity, effectively eliminating false signals in NO_2 detection caused by H_2O interference. This material features ordered modification with predesigned imidazole-amino groups as active sites, demonstrating improved recoverability and recyclability while retaining high sensitivity and selectivity.

1. Introduction

Two-dimensional (2D) materials demonstrate significant potential in stimuli-responsive applications due to their high specific surface area and excellent charge transport properties [1–4]. Compared to conventional 2D materials, the surface of 2D organic-metal chalcogenides (OMCs) is uniformly functionalized with long-range ordered organic functional groups, that offers a high density of programmable active sites for stimuli-responsive interactions, making them particularly attractive for designing advanced gas sensors with molecular-level specificity [5–8]. However, reported OMCs sensing materials typically suffer from sluggish sensing recovery and inadequate cycling performance due to excessive interactions between the sensing-active sites and target gas analytes [9]. Although the recovery can be accelerated through heating or exposing to light to facilitate the desorption of gas molecules, these strategies invariably degrade detection sensitivity while introducing additional device complexities [10]. The design of OMCs sensing materials with rapid recovery capabilities and excellent recyclability remains a critical challenge in this field.

To achieve the goal in designing high performance OMCs sensors with aimed properties, precise control of the interactions between the recognition sites and target molecules is crucial. Thus, an efficient strategy that combines theoretical calculations and experimental synthesis has been developed. As a proof of concept, the development of an OMCs sensor to the hazardous NO_2 has been demonstrated. The hydrogen-bonding interaction between the electron-donating functional groups ($-NH_2$ or -SH) and electron-deficient NO_2 endows such materials with selective detection capabilities for NO_2 [9–12]. However, the excessively strong interaction between these groups and NO_2 impedes rapid desorption of gas molecules from the material. To further reduce sensor recovery time, it is essential to weaken the electron-donating capacity of functional groups on OMCs surfaces, thereby lowering the thermodynamic binding energy and facilitating easier desorption of gas molecules [13–15]. Theoretical calculations reveal that benzimidazole exhibits the lowest binding energy (-2.93 kcal/mol) with NO_2 compared to aniline-type (-6.44 ~ −14.28 kcal/mol) and aliphatic amine-type (~ −3.01 kcal/mol) functional groups (Scheme 1). This weaker binding energy indicates a reduced desorption energy barrier for gas molecules,

---

* Corresponding authors.
E-mail addresses: shiyusheng@fjirsm.ac.cn (Y. Shi), gewang@fjirsm.ac.cn (G. Wang).

https://doi.org/10.1016/j.snb.2025.138577
Received 25 June 2025; Received in revised form 14 August 2025; Accepted 22 August 2025

suggesting potential for rapid and reversible sensing. Consequently, 2-mercaptobenzimidazole (BMT) serves as an excellent model material, functioning as an active site to recognize and mitigate over-interaction with gas molecules, thereby enhancing recovery and recyclability for OMCs sensing materials.

Herein, an imidazole-amino exposed 2D silver-based OMC, AgBMT, was successfully designed and synthesized. In this material, the silver ions coordinate with both the thiol and imine-nitrogen atoms to form the 2D [$Ag_7S_6N_6$] layer. The [$Ag_7S_6N_6$] layers are further interconnected with benzimidazole molecules via S-C and N-C covalent bonds, forming periodically stacked lattices by inorganic and organic layers, while the imidazole-amino groups are regularly distributed outside the 2D [$Ag_7S_6N_6$] layers. AgBMT demonstrates unique selectivity for NO_2, with a response value of 313 % to 10 ppm NO_2 and a limit of detection (LOD) value of 5.3 ppb. In addition, AgBMT exhibits exceptionally fast response (14 s) and recovery times (46 s) to NO_2. Its recovery time ranks among the fastest levels reported so far (typically several minutes for other NO_2 sensors). The CV value of AgBMT is 2.19 %, which is the lowest among reported sensors with recovery times of less than 1 min. Furthermore, AgBMT maintains robust NO_2 sensing performance across a wide humidity range (10–90 % RH), with responses to 10 ppm NO_2 consistently exceeding those in pure relative humidity (RH) conditions. Mechanistic studies reveal that the imidazole-amino groups on the exterior of the 2D layers act as active sites, whose relatively weak electron-donating capability facilitates rapid desorption of adsorbed NO_2 after response. This work establishes a design principle for engineering active sites in sensing materials, offering valuable insights for catalytic, energy storage, and molecular separation etc.

2. Experimental sections

2.1. Materials

This text uses experimental reagents that are all analytical grade and do not require further purification. Silver nitrate ($AgNO_3$, 99.8 %) was purchased from Sinopharm Chemical Reagent Co., Ltd., China. 2-mercaptobenzimidazole (BMT, 99 %) was purchased from Adamas-beta, China. DMF was purchased from Sinopharm Chemical Reagent Co., Ltd., China. Deionized water was produced by Lab ultrapure water system. Ag-Pd interdigital electrode plates with a channel of 200 μm were obtained from Hangzhou Jinbo Tech. Co., Ltd., China. All target gases were sourced from Beijing Hua Yuan Gas Chemical Industry Co., Ltd., China.

2.2. Synthesis of AgBMT

$AgNO_3$ (17 mg) and BMT (30 mg) were mixed in 3 mL methanol (MeOH) and 3 mL N, N-dimethylformamide (DMF), then the mixture was transferred to a 10 mL glass vial reaction vessel and stored at 100 ℃ for 24 h to obtain colourless hexagonal flaky crystals of AgBMT. After cooling to room temperature (25 ℃, RT), it was washed five times with ethanol and placed in a vacuum oven at 60 ℃ overnight.

2.3. Single-crystal X-ray diffraction structure determination

Select clean, unbroken flakes of colourless crystals of AgBMT and place them on the loop. Diffraction data were collected using the ROD Synergy single-crystal diffractometer, which is equipped with a Cu target (Cu Kα, $\lambda = 1.54184$ Å) X-ray source and a Hybrid Pixel area detector. The reduction of the diffraction data was performed using the CrysAlisPro software. The crystal structure was solved using the Olex2 software package, developed by OlexSys. The structure was determined by direct methods using the ShelXT program embedded in Olex2, and full-matrix least-squares refinement was carried out using ShelXT.

2.4. Theoretical Calculations

Density functional theory (DFT) calculations were carried out to investigate the interaction between NO_2 molecules and the ligand. All computations were performed using the DMol3 module in Materials Studio 2020 software (Materials Studio 20.1, BIOVIA, San Diego, CA, USA) [33]. The exchange-correlation interactions were treated using the generalized gradient approximation (GGA) with the Perdew-Burke-Ernzerhof (PBE) functional. A double numerical plus polarization (DNP) basis set was employed, and the self-consistent field (SCF) convergence tolerance was set to 1.0×10^{-6} Ha. Geometry optimizations were performed with fine grid quality until the maximum force was less than 0.002 Ha/Å and the energy change was below 1.0×10^{-5} Ha.

The interaction energy (E_{int}) between a NO_2 molecule and the ligand was calculated using the following equation:

$$E_{\mathrm{int}} = E_{\mathrm{complex}} - (E_{\mathrm{NO2}} + E_{\mathrm{ligand}}) \tag{1}$$

E_{complex} is the total energy of the fully optimized NO_2-ligand, E_{NO2} is the energy of the isolated NO_2 molecule, and E_{ligand} is the energy of the isolated ligand molecule (e.g., benzimidazole, ethylamine, butylamine, etc.), alculated under the same computational conditions (Fig. S1).

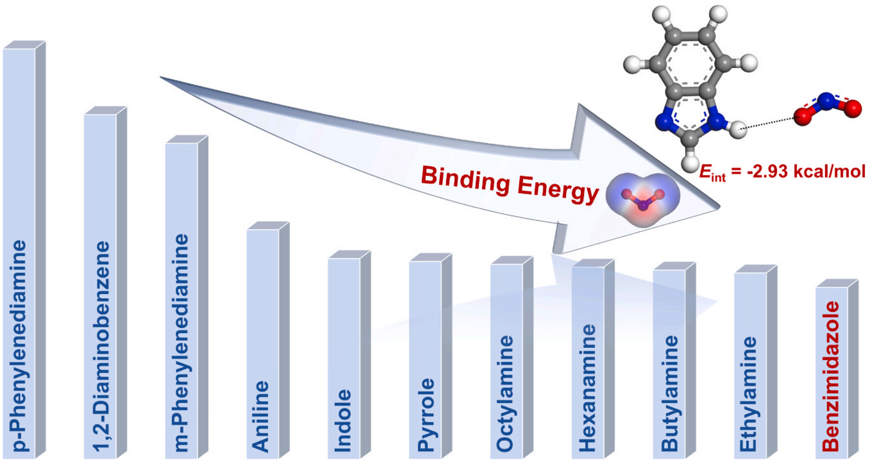

Scheme 1. Binding energies of different amine molecules to NO_2 molecules.

2.5. Characterization methods and test instruments

Powder X-ray diffraction (PXRD) of samples was collected and recorded by Rigaku Smartlab X-ray (Cu Kα_1, $\lambda = 1.5406$ Å) at a scanning speed of 5° min^{-1} (the 2θ range is 3–40° and the step size is 0.02°/ 2θ). The simulated PXRD pattern was generated from the single-crystal structure data using Mercury software (version 1.4.2, developed by the Cambridge Crystallographic Data Centre). During the simulation, the X-ray wavelength, 2θ range, and step size were set to match the experimental conditions to ensure an accurate comparison between the simulated and experimental PXRD patterns. Scanning electron microscope (SEM, ZEISS-300) was operated at 3.0 kV. Transmission electron microscopy (TEM) images were collected on a FEI Talos-F200X G2 field emission transmission electron microscope at an acceleration voltage of 200 kV. The data of X-ray photoelectron spectroscopy (XPS) was collected from a Thermo Scientific ESCALAB 250 Xi XPS system (monochromatic Al Kα X-rays(1486.6 eV) operating at 15 kV; the base pressure: 5.0×10^{-8} Pa). Fourier transform infrared spectroscopy (FTIR) spectra were recorded on a Bruker VERTEX70 FT-IR spectrometer (Germany) in 4000–400 cm^{-1} region using KBr pellets. *In-situ* diffuse reflectance infrared Fourier transform spectroscopy (DRIFTS) experiments were performed on a 6700 Fourier transform-infrared spectrometer (Nicolet) equipped with a stainless steel in-situ IR flow cell and set up for diffuse reflectance sampling. UV-Vis-NIR diffuse reflectance spectra were collected on a Perkin Elmer Lambda 950 spectrophotometer. Barium sulfate powder was used as a non-adsorbing background. Thermogravimetric analysis (TGA) was measured using a NETZSCH STA449F3 analyser (Germany) using an Al_2O_3 crucible with a heating rate of 10 K min^{-1} from 30 to 800 ℃ and a synthetic air flow rate of 20 mL min^{-1}. The electrical measurements were performed using a Keithley 4200 (USA). Gas sensing related electrical tests with Keithley 4200 (USA) and the labVIEW software written by ourselves. Surface areas were measured by nitrogen adsorption and desorption at 77 K using a Bel Japan Inc. model BELSOPR-max analyzer and the samples were degassed at 100 ℃ for 12 h under vacuum (10^{-5} bar) before analysis. The resonant microcantilever is produced by Xiamen High-End MEMS Technology Co., Ltd.

2.6. Measurement of gas sensor

Sensing performances of AgBMT toward all gases were evaluated in a homemade instrument system developed in our early work. As shown in Fig. S2, the system consists of piping, a gas mixing device, a test chamber and a digital source meter. Target gas was introduced into the quartz tube by mixing the certified gas "mixtures" (Beijing Hua Yuan Gas Chemical Industry Co., Ltd., China) and dry air in a proper ratio controlled by the mass flow controllers (CS-200C, Beijing Sevenstar Qualiflow Electronic Equipment Manufacturing Co., Ltd., China). All certified gases were standard gas mixtures (typically 100 ppm of target gas balanced with dry air); no 100 % pure gases were used in this work. Specifically, the NO_2 gas used in the tests was a dry gas mixture of 100 ppm NO_2 balanced with dry air. The constant flow was 200 mL min^{-1}, the bias on the sensor was 5 V and the current was recorded using Keithley 4200 (USA) Sourcemeter. For humidity test, it was precisely regulated by mixing dry air with humidified air using a humidity control system. The voltage was 1 V during the humidity sensitivity test. To simulate the actual operating conditions of the device, synthetic air (79 % nitrogen + 21 % oxygen) was used as the purge and standard carrier gas. The purge gas was introduced for 1 h prior to the test to remove any other gas molecules that might be adsorbed on the material surface and to stabilize the baseline. All tests were performed at RT with all gases at a concentration of 100 ppm.

2.7. Calculations of response, response / recovery time and coefficient of variation

The ratio of current in the target gas atmosphere (I_1) to air current (I_0) is set as the response value (R):

$$R_{response} = (I_1 / I_0 - 1) \times 100\% \tag{2}$$

The response time of the sensor is the time required increasing the response to 90 % of the saturation value and the recovery time is the time required decreasing the response to its 10 %.

The coefficient of variation (CV) is defined as:

$$\mathrm{CV} = \mathrm{R_{SD}} / \mathrm{R_{average}} \times 100\% \tag{3}$$

where $\mathrm{R_{SD}}$ and $\mathrm{R_{average}}$ are the standard deviation (SD) and average value of responses with four successive cycles.

3. Results and discussion

3.1. Materials characterization

Single crystal samples of AgBMT were synthesized using a simple solvothermal method from its MeOH and DMF solutions. Based on the single-crystal X-ray diffraction, AgBMT crystallizes in the centrosymmetric space group R$\overline{3}$ (No. 148), with cell parameters of $a = 13.2060(5)$ Å, $b = 13.2060(5)$ Å, $c = 47.1885(17)$ Å, $\alpha = \beta = 90°$, $\gamma = 120°$, $V = 7127.0(5)$ Å^3 (detailed crystallographic information was demonstrated in Table S1). It features three distinct Ag^+ coordination modes (Fig. 1a): Ag1 in a tetrahedral geometry coordinated by three S atoms and one N atom, Ag2, and Ag3 in trigonal planar configurations, with Ag2 bonded to two S atoms and one N atom, Ag3 bonded by three S atoms. These units are interconnected through edge-sharing, forming a 2D layer. The BMT ligands are regularly distributed outside of the 2D inorganic layer, leaving the uncoordinated imidazole-amino (N-H) groups as the active sites (Fig. S3). The bond lengths of Ag-S, Ag-N, S-C, and N-C bonds fall into the range of 2.419(2)-2.645(2) Å, 2.208(6)-2.246(7) Å, 1.721 (9)-1.730 (9) Å, and 1.335(11)-1.401(12) Å (Table S2). In addition, S-Ag-N and S-Ag-S angles range from 101.74°-133.57° and 92.35°-95.10°, respectively (Table S3). The phase purity of AgBMT was confirmed by the powder XRD pattern (Fig. 1b), in which the experimental pattern agrees well with the simulated one generated from the single-crystal data using Mercury software. Fourier-transform infrared (FT-IR) spectra confirm the disappearance of the -SH stretching vibration at 2550 cm^{-1} [16,17], indicating the coordination between the ligand and metal ions (Fig. 1c). XPS was also conducted to further confirm the chemical states and coordination environments of AgBMT. As presented in Fig. 1d and Fig. S4, the spectrum clearly displays signals for Ag 3*d*, S 2*p*, N 1 *s*, and C 1 *s*. The Ag 3*d* spectrum, analysis shows distinct Ag $3d_{5/2}$ and Ag $3d_{3/2}$ peaks at 367.78 eV and 373.75 eV, respectively, unambiguously verifying the + 1 valence state of Ag[9]. The fine spectrum of S 2*p* exhibits two major peaks at 163.30 eV and 162.12 eV, which are attributed to S $2p_{1/2}$ and S $2p_{3/2}$. Furthermore, the N 1 *s* spectrum gave two peaks at 398.20 and 399.74 eV, which can be attributed to Ag-N and pyrrolic N[18], verifying that the pyridinic N on the imidazole ring forms an Ag-N bond through coordination with Ag, while the pyrrole N (C-NH-C) is not coordinated. SEM measurement unveils a hexagonal sheet-like morphology (Fig. 1e). Additionally, elemental mapping via energy-dispersive X-ray spectroscopy (EDS) validated the uniform distribution of Ag, S, N, and C elements (Fig. S5). Cross-sectional high-resolution transmission electron microscopy (HRTEM) image shows clear superlattice fringe with a space of 1.60 nm, which is consistent with the thickness of an individual layer (1.57 nm) (Fig. S6)[12,19]. Elemental analysis further corroborates the structure and purity of the compound (Table S4).

To further evaluate its potential for practical applications, a series of assessments concerning the semiconductor properties and the stability

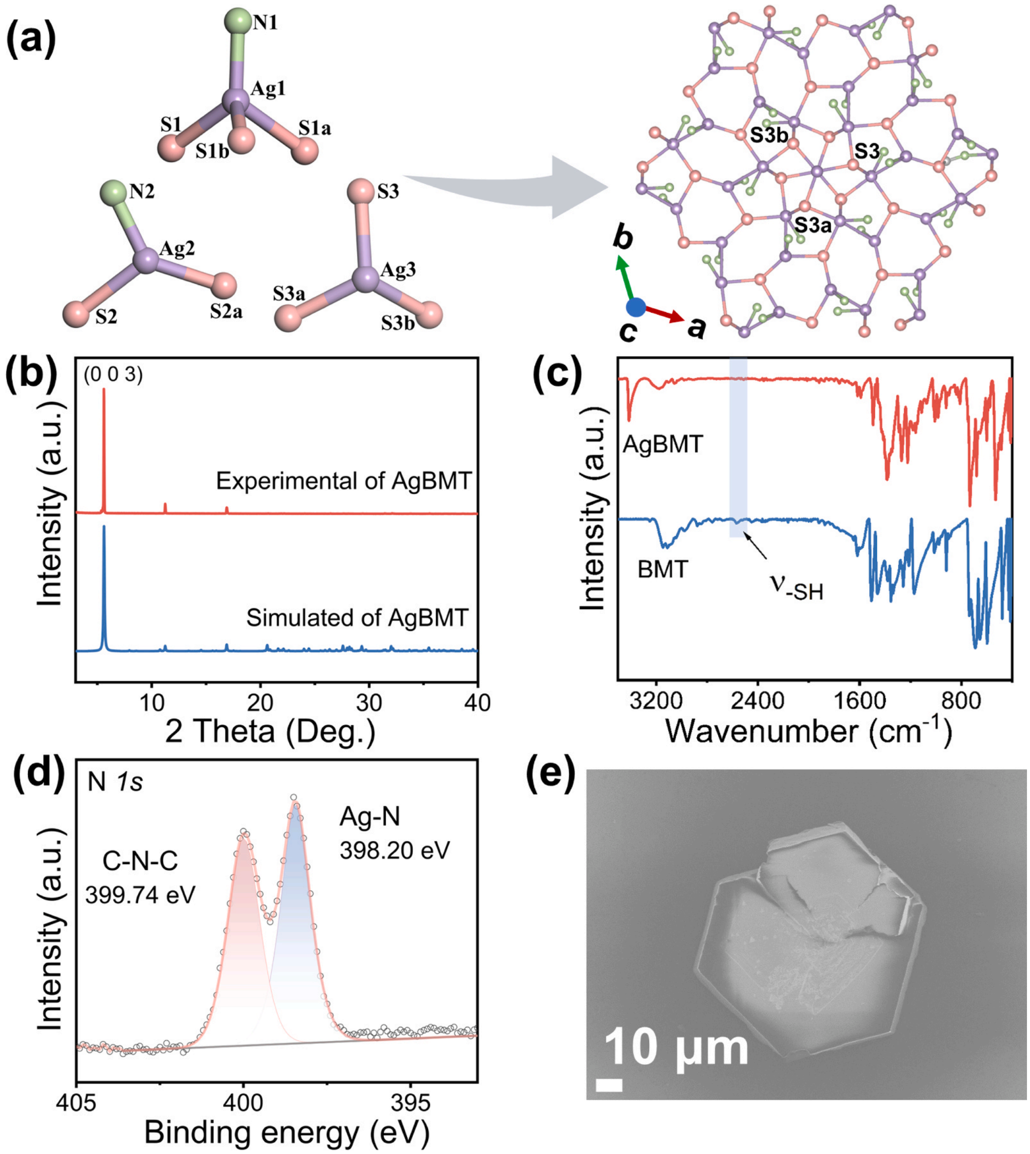

Fig. 1. (a) [$Ag_7S_6N_6$] layer in AgBMT. (b) Experimental and simulated PXRD patterns of AgBMT. (c) FT-IR spectra of AgBMT and BMT. (d) XPS spectrum of N1s. (e) SEM image of AgBMT.

of AgBMT are conducted. PXRD measurements indicate that AgBMT remained intact after immersion in six common solvents for 24 h (Fig. S7). Additionally, the PXRD patterns remained unchanged after storage under RT conditions for three months, demonstrating excellent long-term structural stability (Fig. S8). TGA shows that AgBMT remained stable at 340 ℃ under air or N_2 flow with almost no significant mass loss (Fig. 2a). The optical bandgap of AgBMT, was determined to be 2.56 eV (Fig. 2b) using ultraviolet-visible diffuse reflectance spectroscopy (UV-Vis). The p-type semiconductor nature of AgBMT was confirmed through complementary ultraviolet photo electron spectroscopy (UPS) measurements of the valence band position (Figs. 2c, and 2d), following the same determination method in literature[11]. The semiconductor properties of AgBMT were characterized by the standard two-probe method. I-V curves of AgBMT at different temperatures show linear contours, indicating ohmic contact between the sample and the electrode (Fig. 2e) [20]. The conductivity of AgBMT is 3×10^{-12} S cm^{-1} at RT and increases with the increase of temperature. The good linear relationship of $\ln\sigma \sim 1000/T$ yields an activation energy of 0.732 eV and confirms the semiconductor characteristics of AgBMT (Fig. 2f) [7,21].

3.2. *Gas sensing properties*

The sensors were fabricated by depositing AgBMT onto interdigitated electrodes using a drop-casting technique (Fig. 3), with current signals recorded in response to various gas analytes. All measurements were performed at ambient temperature, utilizing air as the carrier gas, and NO_2 detection was facilitated through the gas sensing system (Fig. S2)[22]. As shown in Fig. 4a, the response of AgBMT to 10 ppm NO_2 is 311 %. Meanwhile, AgBMT exhibits a broad detection range from 0.04 to 100 ppm NO_2, with remarkable sensitivity and response consistency (Fig. S9). The LOD value is calculated to be 5.3 ppb by setting the response to 0.1, which is much below the NO_2 limit required by the World Health Organization (WHO) (Fig. 4b)[23,24]. Notably, when being exposed to 10 ppm NO_2, AgBMT rapidly reaches the response saturation within 14 s, and subsequent recovery in dry air finishes within 46 s (Fig. 4c), superior to most reported NO_2 sensors (Table S5). AgBMT performs an expected selectivity, which effectively discriminates NO_2 from 15 other interfering gases with cross-sensitivities, including acetone, toluene, CO_2, SO_2, and H_2S (Fig. 4d).

Currently reported NO_2 sensors typically exhibit long recovery times ranging from several minutes to tens of minutes, along with excessively

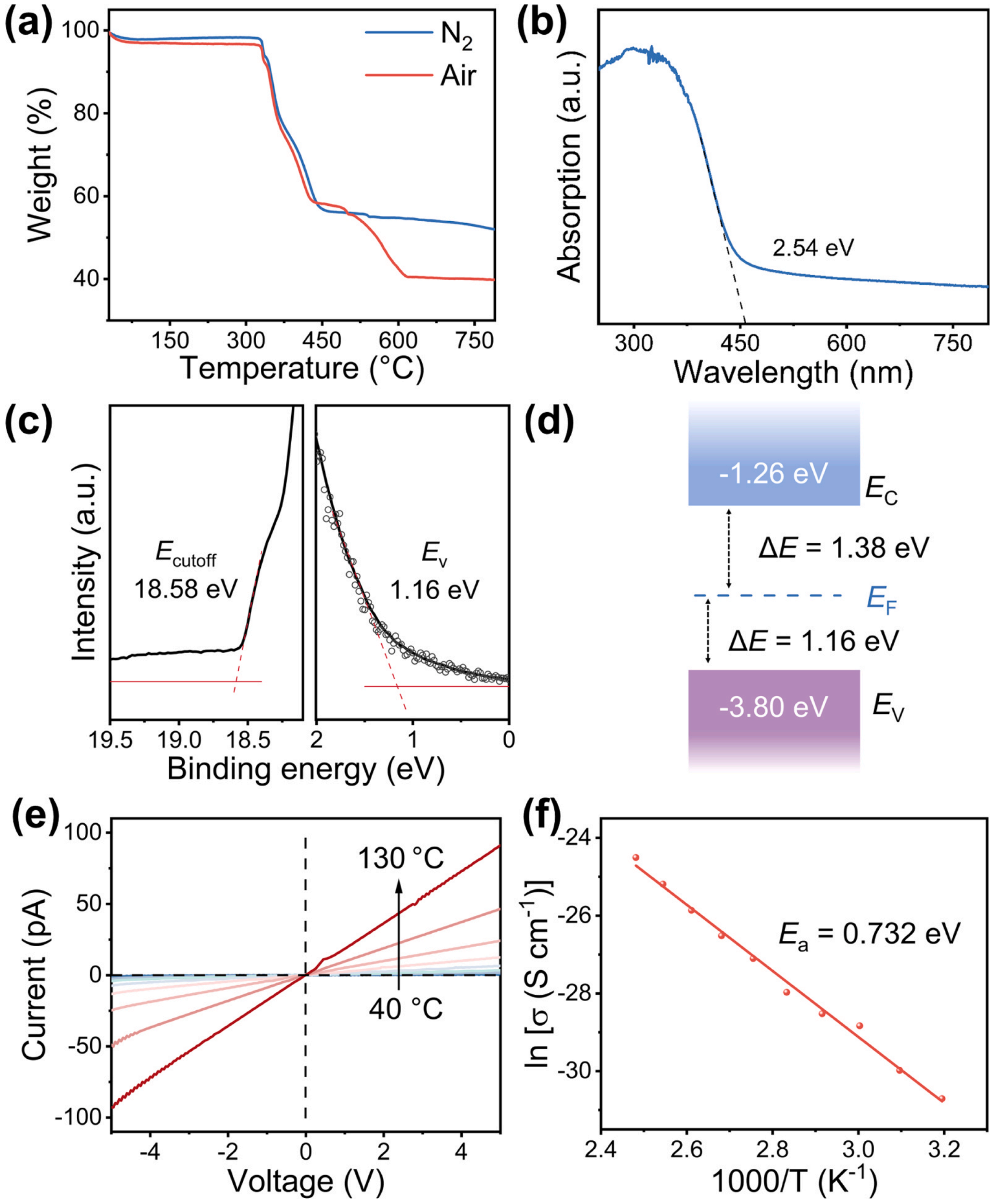

Fig. 2. Basic characterization of AgBMT: (a) TG curve. (b) UV–vis spectra. (c) The secondary electron cut-off edge measured with He I (hν = 21.22 eV) and valence band of AgBMT with respect to the Fermi level (EF = 0). (d) Band structure of AgBMT. (e) Temperature-dependent I-V curves. (f) Arrhenius plots of conductivity.

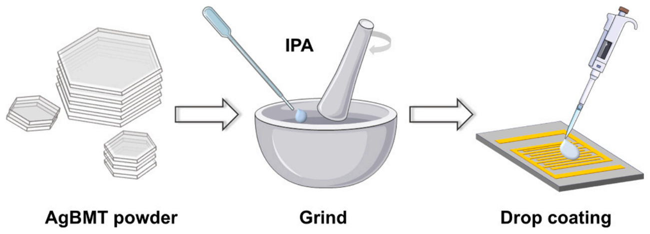

Fig. 3. Fabrication of AgBMT sensors for gas sensitivity testing.

high CV values. The recovery time of AgBMT is shorter than that of 95 % of RT NO_2 sensing materials (Fig. S10). Besides, AgBMT demonstrates a remarkably low CV of only 2.19 % across four consecutive sensing cycles at 10 ppm NO_2, which is the lowest among all reported NO_2 sensors with recovery times of less than 1 min. The low of CV value and short recovery time confirms its exceptional cyclic stability (Fig. 4e)[25]. The structure stability under operating conditions is confirmed by PXRD. After exposure to NO_2, the PXRD of AgBMT remains consistent with the initial one (Fig. S11). Overall, compared with the comprehensive sensing parameters (including response value, CV, response/ recovery time, and LOD values) of other chemiresistive NO_2 sensing materials, AgBMT exhibits rapid recoverability and recyclability while maintaining high sensitivity and selectivity, thus standing out as one of the best RT chemiresistive NO_2 sensing materials reported to date (Table S5). No obvious changes in response were observed after 15 days, demonstrating that AgBMT holds a good long-term stability (Fig. S12). The Brunauer-Emmett-Teller (BET) gas adsorption analysis revealed an exceptionally low nitrogen adsorption capacity, consistent with the non-porous structure of AgBMT (Fig. S13). These results suggest that the drop-casting process does not introduce significant stacking-induced pores, and adsorption/desorption of NO_2 mainly occurs on the external surfaces of the nanosheets.

In practical applications, the sensing performance must be evaluated

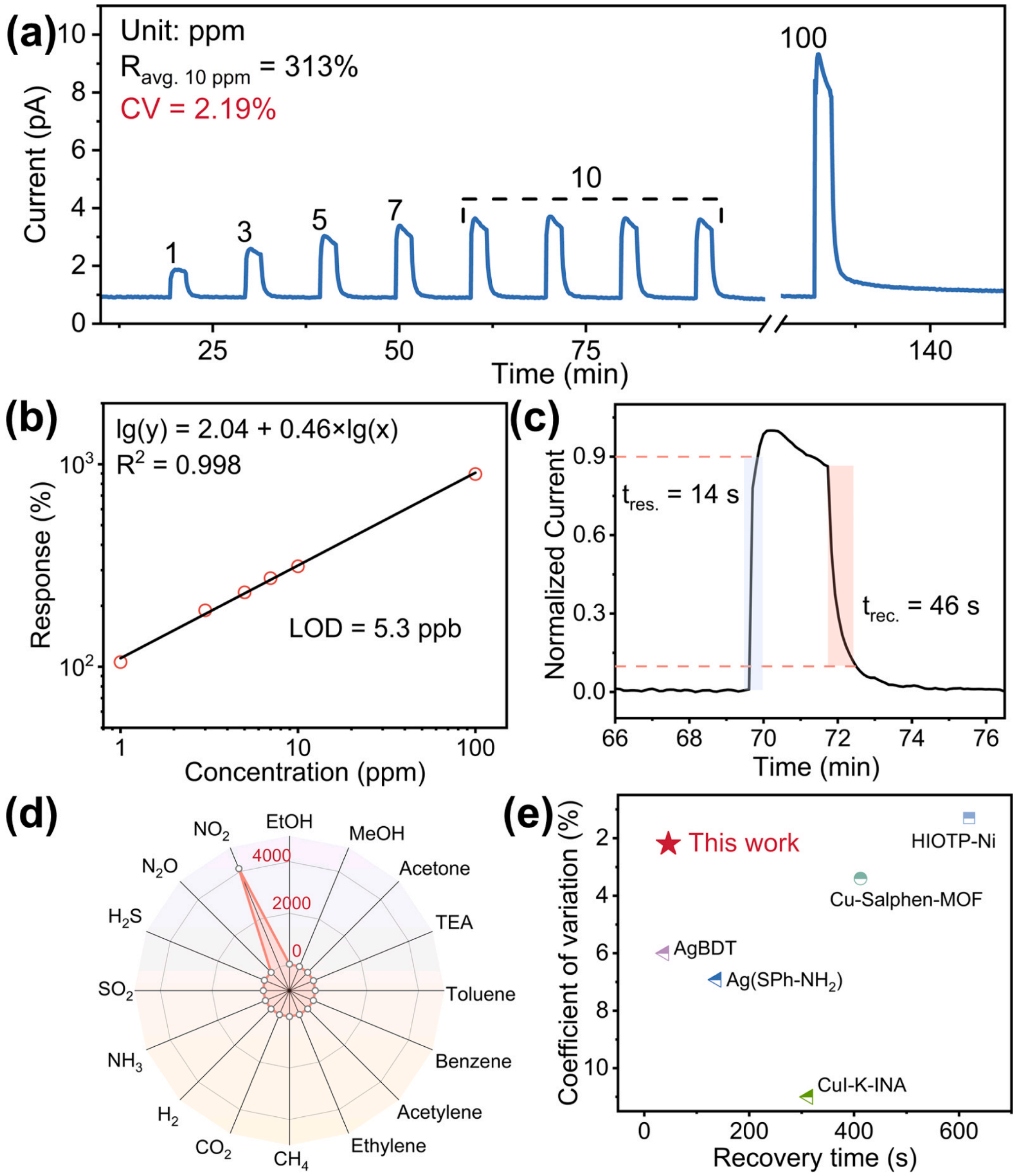

Fig. 4. AgBMT sensor: (a) Response and recovery curve towards NO_2 with different concentrations at RT. (b) Log-log linear fitting of the response-concentration plot. (c) Response and recovery time towards 10 ppm NO_2. (d) Selectivity ratio towards 15 interference gases (100 ppm). (e) Recovery time and CV comparison of AgBMT with the reported CPs NO_2 sensors at room temperature.

in ambient air with controlled RH variations. Thus, the effect of RH on the NO_2 sensing properties of AgBMT has also been studied. As shown in Fig. 5a, the sensor exhibited no observable response under pure humidity conditions in the range of 10–90 % RH, indicating excellent humidity resistance. This performance may be attributed to the orderly arrangement of hydrophobic benzene rings on the surface of AgBMT, which effectively shield the active sites through steric hindrance, thereby minimizing water molecule adsorption. The responses of the

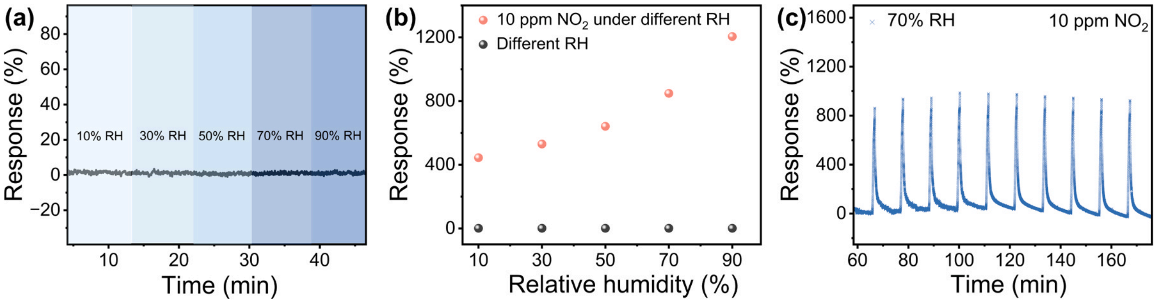

Fig. 5. (a) The response curve of AgBMT under conditions of 10 %-90 % relative humidity. (b) Response of the AgBMT sensor to 10 ppm NO_2 under different humidity conditions and comparison with pure humidity exposure. (c) Cyclic response of the sensor to 10 ppm NO_2 under 70 % relative humidity.

device toward 10 ppm NO_2 under RH range of 10–90 % are obviously higher than those in corresponding pure RH condition, and the response increases with increasing humidity (Fig. 5b). Moreover, AgBMT exhibited good repeatability and cycling stability toward 10 ppm NO_2 under high-humidity (70 % RH) conditions, maintaining a response-recovery rate exceeding 99 % throughout 10 cycles of continuous operation, which also confirms the high feasibility of AgBMT gas sensor for RT NO_2 detection (Fig. 5c).

Although the physical size of H_2O molecule is much smaller than that of NO_2, the hydrophobic interaction of the benzene ring with water will significantly reduce its penetration efficiency. This results in weak adsorption or no adsorption of H_2O. To verify this claim, we used a MEMS resonant micro-suspension beam gas sensor to test the adsorption of H_2O vapor and NO_2 of AgBMT. The adsorption tests reveal that AgBMT demonstrates selective gas uptake at room temperature, with a significantly higher adsorption capacity for NO_2 (18.23 μmol/g at 10 ppm) compared to water vapor (6.09 μmol/g at 25 % RH), despite the much lower NO_2 concentration (Fig. S14). As for the increased response of the NO_2 varying RH conditions, this phenomenon has been reported in previous studies[26–28]. This phenomenon may be stem from humidity-dependent NO_2 hydrolysis, producing reactive intermediates (HNO_3/NO/NO_3) that compete for surface active sites. With the increase of moisture levels, both NO_2 and NO_3 co-exist, and NO_3 molecules become dominant under high humidity conditions. The higher binding energy of NO_3 with sensitive materials than that of NO_2 molecules may contribute to the increased response of the sensor at higher humidity levels. Additionally, the DFT calculations [29] also reveal the enhanced NO_2 adsorption and charge transfer in the presence of humidity. Thus, the response to NO_2 increases as the RH rises.

3.3. Sensing mechanism

The potential energy map indicates that the imidazole-amino group on the surface of the material is the main adsorption site for NO_2 (Fig. 6a). DRIFTS measurements were performed to elucidate the sensing mechanism. As depicted in Fig. 6b, a series of new peaks were observed for AgBMT after being exposed to NO_2 with respect to the spectrum of the pristine sample. The intensities of these bands continue to increase as a function of exposing time, indicating that they correspond to the species produced by interaction/reaction with NO_2 on the sample surface. The imidazole-amino vibration (3402 cm^{-1}) decreased sharply, which further proves that imidazole-amino is the active site for NO_2. New peaks belonging to the NO_2 symmetric and asymmetric stretching vibrations peaks (1619, 1525, 1324, and 1246 cm^{-1}) and the NO_2 bending vibrations peaks (1459 and 1132 cm^{-1}) were observed, indicating the adsorption of NO_2 to AgBMT[29,30]. Additionally, the presence of NH···O bending modes (2500–3000 cm^{-1}) the FTIR spectrum indicated hydrogen bonding between NO_2 and amino-H atoms upon NO_2 exposure[31,32]. Upon introduction of fresh air, the weakening of characteristic imidazole-amino group vibrations (Fig. S15) indicated progressive NO_2 desorption from the material. The identical FT-IR spectra observed before and after NO_2 exposure (Fig. S16) demonstrates complete desorption of all adsorbed NO_2 molecules. This spectral reversibility supports the recyclable nature of the material.

Based on the above discussion, the sensing mechanism can be described as follows (Fig. 6c): When NO_2 molecules approach the surface of AgBMT, the densely and orderly dispersed imidazole-amino groups offer abundant recognition sites for the rapid capture of the NO_2 gas molecules. As a p-type semiconductor, during this process, charge transfer occurs from AgBMT to NO_2, leading to an increase in the concentration of hole carriers in AgBMT, which in turn causes a rise in current, demonstrating a positive response signal. Simultaneously, due to the relatively weak electron-donating ability of the imidazole-amino recognition groups, the thermodynamic binding energy with NO_2 is reduced, weakening the interaction between NO_2 molecules and the material surface. This facilitates the desorption process of NO_2 molecules, significantly shortening the recovery time of the sensor. Therefore, upon completion of detection, NO_2 molecules can quickly be

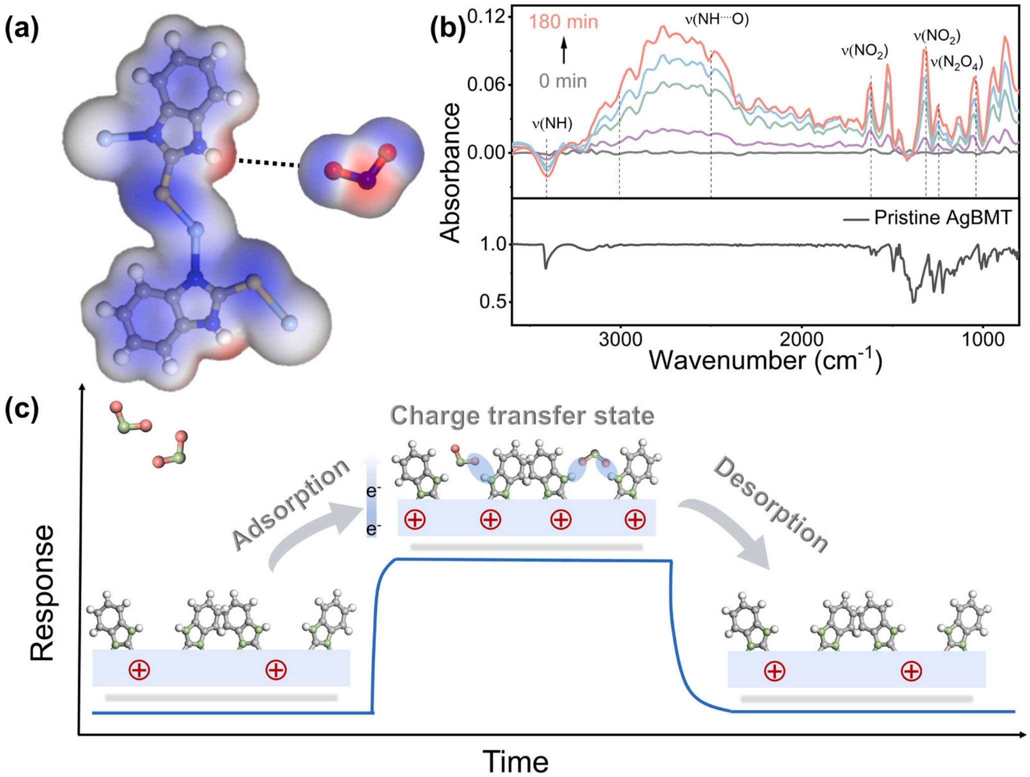

Fig. 6. (a) Surface electrostatic potential distribution of AgBMT and NO_2. (b) In situ DRIFT Spectra for AgBMT exposed to NO_2 as a function of time. (c) Possible NO_2 sensing mechanism for AgBMT.

released from the material surface, and once the NO_2 on the AgBMT surface is cleared by air, the current rapidly returns to its initial value.

4. Conclusions

In summary, we exhibited an imidazole-amino modified 2D OMC, AgBMT, to accelerate the recovery speed during NO_2 detection. The relatively weak interactions between imidazole-amino groups and NO_2 enable efficient desorption process after detection, significantly enhancing the recovery performance. The AgBMT exhibits excellent dynamic response characteristics with recovery time (46 s), superior to most reported NO_2 sensors (typically over several minutes for others). Its CV value is as low as 2.19 %, which is the lowest among all reported NO_2 sensors with recovery times of less than 1 min, demonstrating its excellent cycling stability. Moreover, it specifically responses to NO_2 in 15 common interfering gases, showing excellent selectivity. Importantly, AgBMT also exhibits excellent humidity resistance, which is critical for practical applications. This work provides a versatile platform for functional group engineering and weak interaction optimization in creating advanced functional materials, with broad implications for catalysis, sensing, separation, and related fields.

CRediT authorship contribution statement

Wei Gong: Writing – original draft, Formal analysis, Data curation. **Yu Pan:** Formal analysis. **Guane Wang:** Writing – review & editing, Supervision, Funding acquisition. **Gang Xu:** Writing – review & editing, Funding acquisition. **Yusheng Shi:** Writing – review & editing, Funding acquisition.

Declaration of Competing Interest

The authors declare the following financial interests/personal relationships which may be considered as potential competing interests. Guane Wang reports financial support was provided by National Natural Science Foundation of China. Guane Wang reports financial support was provided by Fujian Science & Technology Innovation Laboratory for Optoelectronic Information of China. Guane Wang reports financial support was provided by Natural Science Foundation of Fujian Province. Yusheng Shi reports financial support was provided by National Natural Science Foundation of China. If there are other authors, they declare that they have no known competing financial interests or personal relationships that could have appeared to influence the work reported in this paper.

Acknowledgments

This work was financially supported by the National Natural Science Foundation of China (22422508, 22271281, 22325109, 22171263, 22301028, and 62227815), Fujian Science & Technology Innovation Laboratory for Optoelectronic Information of China (2021ZR101) and the Natural Science Foundation of Fujian Province (2022J06032), Self-deployment Project Research Program of Haixi Institutes, Chinese Academy of Sciences (CXZX-2022-GH09, CXZX-2022-JQ03, CXZX-2023-GS03), Strategic Priority Research Program of the Chinese Academy of Sciences (XDB 1170000).

Declaration of competing interest

The authors declare that they have no known competing financial interests or personal relationships that could have appeared to influence the work reported in this paper.

Appendix A. Supporting information

Supplementary data associated with this article can be found in the online version at doi:10.1016/j.snb.2025.138577.

Data availability

Data will be made available on request.

References

[1] S. Yuan, S. Zhang, Recent progress on gas sensors based on graphene-like 2D/2D nanocomposites, J. Semicond. 40 (2019) 111608–111623, https://doi.org/10.1088/1674-4926/40/11/111608.

[2] S. Liu, X.T. Pan, H.Y. Liu, Two-Dimensional nanomaterials for photothermal therapy, Angew. Chem. Int. Ed. 59 (2020) 5890–5900, https://doi.org/10.1002/anie.201911477.

[3] J. Orangi, M. Beidaghi, A review of the effects of electrode fabrication and assembly processes on the structure and electrochemical performance of 2D MXenes, Adv. Funct. Mater. 30 (2020) 2005305–2005327, https://doi.org/10.1002/adfm.202005305.

[4] X.H. Liu, T.T. Ma, N. Pinna, J. Zhang, Two-dimensional nanostructured materials for gas sensing, Adv. Funct. Mater. 27 (2017) 1702168–1702198, https://doi.org/10.1002/adfm.201702168.

[5] G.E. Wang, S.Z. Luo, T. Di, Z.H. Fu, G. Xu, Layered organic metal chalcogenides (OMCs): from bulk to two-dimensional materials, Angew. Chem. Int. Ed. 61 (2022) e202203151, https://doi.org/10.1002/anie.202203151.

[6] Y. Pan, C.P. Wang, Z.H. Fu, G.E. Wang, G. Xu, Fluorescence sensing of nitrophenol explosives using a two-dimensional organic-metal chalcogenide fully covered with functional groups, Chem. Commun. 58 (2022) 4615–4618, https://doi.org/10.1039/d2cc00834c.

[7] Y.Z. Li, X.M. Jiang, Z.H. Fu, Q.Q. Huang, G.E. Wang, W.H. Deng, C. Wang, Z.Z. Li, W.J. Yin, B.L. Chen, G. Xu, Coordination assembly of 2D ordered organic metal chalcogenides with widely tunable electronic band gaps, Nat. Commun. 11 (2020) 261–270, https://doi.org/10.1038/s41467-019-14136-8.

[8] Y.Z. Li, J. Shu, Q.Q. Huang, K. Chiranjeevulu, P.N. Kumar, G.E. Wang, W.H. Deng, D.P. Tang, G. Xu, 2D metal chalcogenides with surfaces fully covered with an organic "promoter" for high-performance biomimetic catalysis, Chem. Commun. 55 (2019) 10444–10447, https://doi.org/10.1039/c9cc03443a.

[9] H.J. Jiang, L.N. Cao, Y.Z. Li, W.H. Li, X.L. Ye, W.H. Deng, X.M. Jiang, G.N. Wang, G. Xu, Organic "receptor" fully covered few-layer organic-metal chalcogenides for high-performance chemiresistive gas sensing at room temperature, Chem. Commun. 56 (2020) 5366–5369, https://doi.org/10.1039/d0cc01092h.

[10] G. Jung, H. Shin, S.W. Jeon, Y.H. Lim, S. Hong, D.H. Kim, J.H. Lee, Transducer-Aware Hydroxy-Rich-Surface indium oxide gas sensor for Low-Power and High-Sensitivity NO_2 gas sensing, ACS Appl. Mater. Interfaces 15 (2023) 22651–22661, https://doi.org/10.1021/acsami.3c00022.

[11] G.N. Liu, X.N. Tang, J.S. Guo, Q.S. Liu, C. Ye, C.C. Li, G. Xu, G.E. Wang, An unprecedented three-dimensional copper-halide-sulfur semiconductive framework for effective light and nitrogen dioxide electrical detections, Sens. Actuator BChem. 399 (2024) 134864–134872, https://doi.org/10.1016/j.snb.2023.134864.

[12] Y.Y. Wen, G.E. Wang, X.M. Jiang, X.L. Ye, W.H. Li, G. Xu, A covalent organic-inorganic hybrid superlattice covered with organic functional groups for highly sensitive and selective gas sensing, Angew. Chem. Int. Ed. 60 (2021) 19710–19714, https://doi.org/10.1002/anie.202107185.

[13] G. Garrido, E. Koort, C. Ràfols, E. Bosch, T. Rodima, I. Leito, M. Rosés, Acid-base equilibria in nonpolar media. Absolute pK_a scale of bases in tetrahydrofuran, J. Org. Chem. 71 (2006) 9062–9067, https://doi.org/10.1021/jo061432g.

[14] S.P. Porras, M.L. Riekkola, E. Kenndler, Capillary zone electrophoresis of basic analytes in methanol as non-aqueous solvent-mobility and ionisation constant, J. Chromatogr. A 905 (2001) 259–268, https://doi.org/10.1016/s0021-9673(00)00981-x.

[15] L. Sooväli, T. Rodima, I. Kaljurand, A. Kütt, I.A. Koppel, I. Leito, Basicity of some P_1 phosphazenes in water and in aqueous surfactant solution, Org. Biomol. Chem. 4 (2006) 2100–2105, https://doi.org/10.1039/b602797k.

[16] H.C. Jie, Z.Q. Lan, K.F. Li, X.L. Ye, S.L. Duan, Z.H. Fu, G.E. Wang, G. Xu, Surface functionalized chalcogenides for highly selective removal of Hg^{2+}, CrystEngComm 26 (2024) 6255–6259, https://doi.org/10.1039/d4ce00923a.

[17] C.H. Yu, X.X. Zhu, K.F. Li, G.E. Wang, G. Xu, 1D p-type molecular-based coordination polymer semiconductor with ultrahigh mobility, Sci. Bull. 69 (2024) 2705–2711, https://doi.org/10.1016/j.scib.2024.07.006.

[18] B.G. Kim, D.N. Nguyen, W. Jang, J.K. Kim, D.H. Wang, Formulation of conductive nanocomposites by incorporating silver-doped carbon quantum dots for efficient charge extraction, Int. J. Energy Res. 45 (2021) 21324–21339, https://doi.org/10.1002/er.7183.

[19] C. Sun, K. Liu, J. Zhang, Q. Liu, X.J. Liu, L.L. Han, *in situ* transmission electron microscopy and Three-Dimensional electron tomography for catalyst studies, Chin. J. Struct. Chem. 41 (2022) 2210056–2210076, https://doi.org/10.14102/j.cnki.0254-5861.2022-0187.

[20] Z.F. Wu, C.Z. Wang, X.W. Liu, K. Tan, Z.H. Fu, S.J. Teat, Z.W. Li, X.Z. Hei, X. Y. Huang, G. Xu, J. Li, Confinement of 1D chain and 2D layered CuI modules in K-INA-R frameworks via coordination assembly: structure regulation and semiconductivity tuning, J. Am. Chem. Soc. 145 (2023) 19293–19302, https://doi.org/10.1021/jacs.3c05095.

[21] S. Sibilia, F. Bertocchi, S. Chiodini, F. Cristiano, L. Ferrigno, G. Giovinco, A. Maffucci, Temperature-dependent electrical resistivity of macroscopic graphene

nanoplatelet strips, Nanotechnology 32 (2021) 275701–275712, https://doi.org/10.1088/1361-6528/abef95.

[22] M.S. Yao, W.X. Tang, G.E. Wang, B. Nath, G. Xu, MOF thin Film-Coated metal oxide nanowire array: significantly improved chemiresistor sensor performance, Adv. Mater. 28 (2016) 5229–5234, https://doi.org/10.1002/adma.201506457.

[23] Z.J. Li, Y.Y. Liu, D.F. Guo, J.J. Guo, Y.L. Su, Room-temperature synthesis of cuo/reduced graphene oxide nanohybrids for high-performance NO_2 gas sensor, Sens. Actuator BChem. 271 (2018) 306–310, https://doi.org/10.1016/j.snb.2018.05.097.

[24] M.Y. Hu, Y.A. Chen, D.H. Yuan, R. Yu, X.C. Lu, J.C.H. Fung, W.Y. Chen, Y. Q. Huang, A.K.H. Lau, Estimation and spatiotemporal analysis of NO_2 pollution in east Asia during 2001-2016, J. Geophys. Res. Atmos. 127 (2022) e2021JD035129, https://doi.org/10.1029/2021jd035129.

[25] Y. Lin, W.H. Li, Y.Y. Wen, G.E. Wang, X.L. Ye, G. Xu, Layer-by-Layer growth of Preferred-Oriented MOF thin film on nanowire array for High-Performance chemiresistive sensing, Angew. Chem. Int. Ed. 60 (2021) 25758–25761, https://doi.org/10.1002/anie.202111519.

[26] F. Yao, L.D. Dinh, S.C. Lim, S.B. Yang, H.R. Hwang, W.J. Yu, I.H. Lee, F. Günes, Y. H. Lee, Humidity-assisted selective reactivity between NO_2 and SO_2 gas on carbon nanotubes, J. Mater. Chem. 21 (2011) 4502–4508, https://doi.org/10.1039/c0jm03227a.

[27] Y.T. Han, Y. Liu, C. Su, S.T. Wang, H. Li, M. Zeng, N.T. Hu, Y.J. Su, Z.H. Zhou, H. Wei, Z. Yang, Interface engineered WS_2/ZnS heterostructures for sensitive and reversible NO_2 room temperature sensing, Sens. Actuator BChem. 296 (2019) 126666–126675, https://doi.org/10.1016/j.snb.2019.126666.

[28] A.V. Agrawal, A.Y. Polyakov, J. Eriksson, T.J. Antosiewicz, T.O. Shegai, Humidity-Enhanced NO_2 gas sensing using atomically sharp edges in multilayer mo, S_2 Small Struct. 6 (2025) 2400409–2400413, https://doi.org/10.1002/sstr.202400409.

[29] B. Tyagi, C.D. Chudasama, R.V. Jasra, Determination of structural modification in acid activated montmorillonite clay by FT-IR spectroscopy, Spectrochim. Acta Part A. 64 (2006) 273–278, https://doi.org/10.1016/j.saa.2005.07.018.

[30] Q. Liu, Y.Y. Wen, J.Z. Xiao, S.Z. Luo, G.E. Wang, P.Y. Tang, X.L. Ye, G. Xu, Enhanced room temperature gas sensing performance of ZnO with atomic-level pt catalysts facilitated by the polydopamine mediator, Chin. J. Struct. Chem. 42 (2023) 100069–100076, https://doi.org/10.1016/j.cjsc.2023.100069.

[31] E. Flores, J. Viallon, P. Moussay, F. Idrees, R.I. Wielgosz, Highly accurate nitrogen dioxide (NO_2) in nitrogen standards based on permeation, Anal. Chem. 84 (2012) 10283–10290, https://doi.org/10.1021/ac3024153.

[32] C. Yu, H.Z. Lin, J. Zhou, X.F. Cheng, J.H. He, H. Li, Q.F. Xu, N.J. Li, D.Y. Chen, J. M. Lu, An ion-in-conjugation polymer enables the detection of NO_2 with parts-per-trillion sensitivity and ultrahigh selectivity, J. Mater. Chem. A 8 (2020) 1052–1058, https://doi.org/10.1039/c9ta11513g.

[33] Dassault Systèmes BIOVIA. Materials Studio 20.1, Dassault Systèmes, San Diego, 2020.

Wei Gong received her undergraduate degree from Linyi University in 2022. She is currently pursuing postgraduate studies at the Fujian Institute of Research on the Structure of Matter, Chinese Academy of Sciences (mentor: Guan-E Wang). Her research focuses on synthesizing and studying the performance of organic-metal chalcogenides.

Yu Pan received her undergraduate degree from Yangzhou University in 2019. She is currently pursuing her Ph.D. degree at the Fujian Institute of Research on the Structure of Matter, Chinese Academy of Sciences (mentor: Gang Xu). Her research interests focus on porous framework materials and chemiresistive gas sensing materials.

Dr. Yusheng Shi received his Ph.D. degree (2021) and carried on postdoctoral research at Dalian University of Technology, China. He is currently an associate professor at Fujian Institute of Research on the Structure of Matter, Chinese Academy of Sciences. His interest is the design and application of the coordination polymers with photonic and/or electronic properties.

Guan-E Wang earned her PhD in 2013 from Fujian Institute of Research on the Structure of Matter, Chinese Academy of Science (FJIRSM, CAS). She is currently a professor at FJIRSM. Her research interests include gas sensor materials and devices, including porous conductive inorganic-organic hybrids and organic-metal chalcogenides.

Gang Xu received his PhD in 2008 from Fujian Institute of Research on the Structure of Matter (FJIRSM), CAS. He worked as postdoctoral fellow at COSDAF in City University of Hong Kong (Hong Kong), University of Regensburg (Alexander von Humboldt fellowship, Germany) and Kyoto University (JSPS fellowship, Japan). In 2013, he joined FJIRSM and conducted independent research as a PI. His research interests are conductive coordination polymers, thin-film preparation, and electric devices.